Room-temperature X-ray response of cadmium–zinc–telluride pixel detectors grown by the vertical Bridgman technique

Leonardo Abbene,[a]* Fabio Principato,[a] Gaetano Gerardi,[a] Antonino Buttacavoli,[a] Donato Cascio,[a] Manuele Bettelli,[b] Nicola Sarzi Amadè,[b] Paul Seller,[c] Matthew C. Veale,[c] Oliver Fox,[d] Kawal Sawhney,[d] Silvia Zanettini,[e] Elio Tomarchio[f] and Andrea Zappettini[b]

[a]Dipartimento di Fisica e Chimica (DiFC), University of Palermo, Viale delle Scienze, Edificio 18, 90128 Palermo, Italy, [b]IMEM-CNR, Parco Area delle Scienze 37/A, 43100 Parma, Italy, [c]Rutherford Appleton Laboratory, Science and Technology Facilities Council, Chilton, Oxfordshire OX11 0QX, UK, [d]B16 Beamline, Diamond Light Source, Fermi Avenue, Didcot, UK, [e]due2lab s.r.l., Via Paolo Borsellino 2, Scandiano, 42019 Reggio Emilia, Italy, and [f]Dipartimento di Ingegneria, University of Palermo, Viale delle Scienze, Edificio 7, 90128 Palermo, Italy. *Correspondence e-mail: leonardo.abbene@unipa.it

In this work, the spectroscopic performances of new cadmium–zinc–telluride (CZT) pixel detectors recently developed at IMEM-CNR of Parma (Italy) are presented. Sub-millimetre arrays with pixel pitch less than 500 μm, based on boron oxide encapsulated vertical Bridgman grown CZT crystals, were fabricated. Excellent room-temperature performance characterizes the detectors even at high-bias-voltage operation (9000 V cm^{-1}), with energy resolutions (FWHM) of 4% (0.9 keV), 1.7% (1 keV) and 1.3% (1.6 keV) at 22.1, 59.5 and 122.1 keV, respectively. Charge-sharing investigations were performed with both uncollimated and collimated synchrotron X-ray beams with particular attention to the mitigation of the charge losses at the inter-pixel gap region. High-rate measurements demonstrated the absence of high-flux radiation-induced polarization phenomena up to 2×10^6 photons mm^{-2} s^{-1}. These activities are in the framework of an international collaboration on the development of energy-resolved photon-counting systems for high-flux energy-resolved X-ray imaging.

1. Introduction

The detection of ionizing radiation with solid-state detectors was pioneered by Van Herdeen with AgCl detectors (Van Herdeen, 1945). Since then several high-Z and wide-bandgap compound semiconductors (cadmium telluride, cadmium zinc telluride, mercuric iodide, thallium bromide) have been extensively fabricated and studied for the development of high-resolution room-temperature radiation detectors (Del Sordo *et al.*, 2009; Fougeres *et al.*, 1999; McGregor *et al.*, 1997; Owens *et al.*, 2004; Takahashi *et al.*, 2001; Veale *et al.*, 2014). Cadmium zinc telluride (CdZnTe or CZT) is one of the key materials for radiation detection because of its appealing physical properties (high atomic number, wide band gap, high density) and the continuing advancement of the crystal growth and device-fabrication technologies (Chen *et al.*, 2008; Iniewski, 2014; Szeles *et al.*, 2008). Great efforts have been made to improve the charge-carrier-transport properties of CZT crystals and the electrical contacts of the detectors to reduce incomplete charge collection, electronic noise and high-flux radiation-induced polarization phenomena. Typically, spectroscopic-grade CZT crystals are characterized by
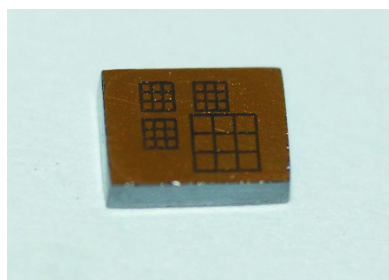
mobility-lifetime products of electrons, $\mu_e\tau_e$, ranging from 10^{-3} cm^2 V^{-1} to 10^{-2} cm^2 V^{-1}, and the detectors, fabricated with quasi-ohmic electrical contacts, allow high-bias-voltage operation (electric field > 2000 V cm^{-1}) and no bias induced polarization (Farella *et al.*, 2009; Principato *et al.*, 2013; Turturici *et al.*, 2014) even at room temperature. In recent years, CZT arrays with sub-millimetre pixelization were proposed for the development of room-temperature energy-resolved photon-counting (ERPC) systems (Barber *et al.*, 2015; Del Sordo *et al.*, 2004; Iwanczyk *et al.*, 2009; Seller *et al.*, 2011; Szeles *et al.*, 2008; Zhang *et al.*, 2007), which are very attractive for next-generation X-ray imaging instrumentation.

Spectroscopic-grade CZT crystals grown by the boron oxide encapsulated vertical Bridgman (B-VB) technique are currently fabricated at IMEM-CNR of Parma, Italy (Abbene *et al.*, 2016; Zappettini *et al.*, 2007, 2009). B-VB CZT detectors, with planar electrode geometry and quasi-ohmic contacts (gold electroless contacts), are characterized by good room-temperature performance (Abbene *et al.*, 2016) and high-bias-voltage operation (electric field up to 10000 V cm^{-1}).

In this work, we will present the first results of a spectroscopic characterization of B-VB CZT detectors with sub-millimetre anode pixelization, recently developed at IMEM-CNR. The room-temperature performance was investigated with both uncollimated and collimated X-ray beams, with particular attention to the charge-sharing and charge-losses effects in the energy spectra.

2. Materials and methods

2.1. Detectors

CZT pixel detectors with different anode arrays were fabricated by IMEM-CNR (http://www.imem.cnr.it) and due2lab s.r.l. (Reggio Emilia, Italy; http://www.due2lab.com). The detectors are based on CZT crystals (4.25 mm × 3.25 mm × 1 mm) grown by the B-VB technique. Gold electroless contacts were realized on both the anode (prepared by using water solutions) and the cathode (prepared by alcoholic solutions) of all CZT samples. The anode surface consists of four arrays of 3 × 3 pixels with pixel pitches of 500 and 250 μm, surrounded by a guard-ring electrode, while the cathode is a planar electrode covering the detector surface (Fig. 1). The width of the inter-pixel gaps for all arrays is equal to 50 μm. Two detectors with the same anode and cathode geometry were tested, showing similar spectroscopic performance.

2.2. Electronics

The pixels of the detectors were DC coupled to analog charge-sensitive preamplifiers (CSPs) and processed by using multichannel digital pulse processing electronics.

The CSPs were based on a fast- and low-noise application-specific integrated circuit (PIXIE ASIC) developed at RAL (Didcot, UK) (Allwork *et al.*, 2012; Veale *et al.*, 2011). The PIXIE ASIC, flip-chip bonded directly to the detector pixels, consists of four arrays of 3 × 3 pixels. The nine outputs from
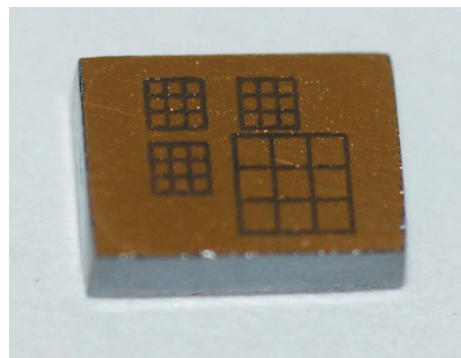
Figure 1
The 1 mm-thick B-VB grown CZT detector (anode side view). The four arrays of 3 × 3 pixels with pixel pitches of 500 and 250 μm are clearly visible.

each of the four arrays are multiplexed onto a common nine track analogue bus which is driven off chip by output buffers. The outputs of all nine pixels of the selected array are read out simultaneously allowing analysis of the height and shape of the pulses. The pulses are characterized by rise times of less than 60 ns and noise (equivalent noise charge) of less than 80 electrons. The bonding process was performed at RAL by using low-temperature curing (<150°C) silver-loaded epoxy and the gold stud bonding technique (Schneider *et al.*, 2015).

The output waveforms from the PIXIE ASIC were digitized and processed online by 16 channel digital electronics, developed at Dipartimento di Fisica e Chimica (DiFC) of the University of Palermo (Italy) (Abbene *et al.*, 2013a,b, 2015b; Gerardi *et al.*, 2014). The digital electronics is based on commercial digitizers (DT5724, 16 bit, 100 MS s^{-1} (mega-samples per second), CAEN S.p.A., Italy; http://www.caen.it), where an original firmware was uploaded (Abbene *et al.*, 2015b; Gerardi *et al.*, 2014). The digital analysis performs the shaping of the output waveform from the detector ASIC by using the classical single-delay line-shaping technique (Knoll, 2000). The delay time acts as the shaping-time constant of a standard shaping amplifier. Moreover, to increase the signal-to-noise ratio we also performed further shaping with a trapezoidal filtering. In this work, we used a delay time of 200 ns.

A detailed description of the digital analysis is reported in our previous works (Abbene *et al.*, 2015b; Gerardi *et al.*, 2014).

2.3. Experimental procedures

The spectroscopic response of the detectors was investigated by using uncollimated radiation sources (^{109}Cd: 22.1, 24.9 and 88.1 keV; ^{241}Am: 59.5 and 26.3 keV; ^{57}Co: 122.1 and 136.5 keV). The ^{57}Co energy spectra also feature the W fluorescent lines produced in the tungsten source backing ($K\alpha_1$ = 59.3 keV, $K\alpha_2$ = 58.0 keV, $K\beta_1$ = 67.2 keV, $K\beta_3$ = 66.9 keV). The source holders shield the 14 keV gamma line of the ^{57}Co source and the Np L X-ray lines of the ^{241}Am source. The detectors were irradiated through the cathode side.

Collimated micro-beams were also used at the B16 test beamline at the Diamond Light Source synchrotron (Didcot,

UK; http://www.diamond.ac.uk/Beamlines/Materials/B16). For these measurements, the storage ring was operated at 3 GeV with a current of 250 mA. Monochromatic X-rays, with energies up to 50 keV, were provided by using a multi-layer monochromator. A 10 µm × 10 µm collimated beam was produced using a set of JJ slits with tungsten carbide blades (JJ X-ray, Hoersholm, Denmark). Two sets of slits were used, one set at the beam entrance which was used to define the beam
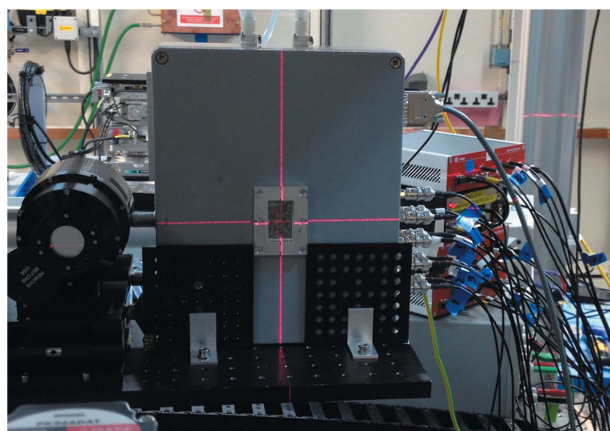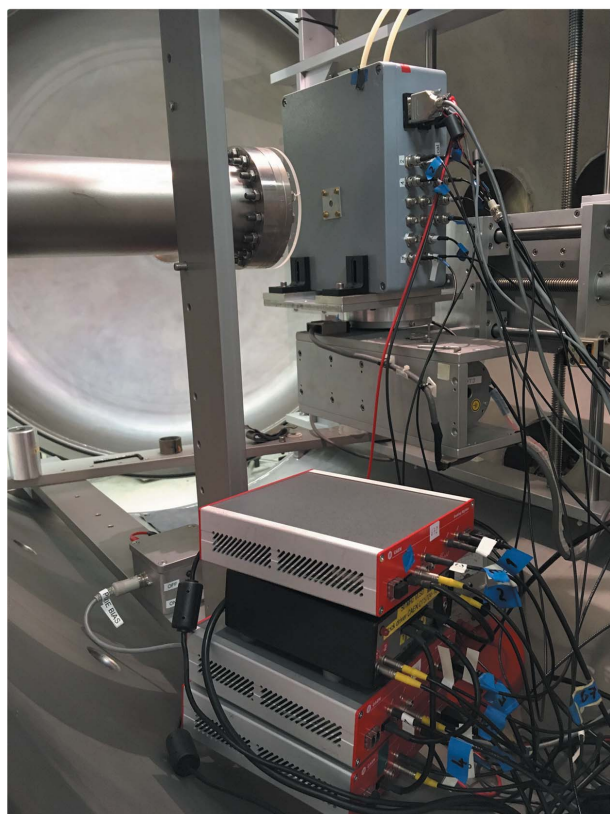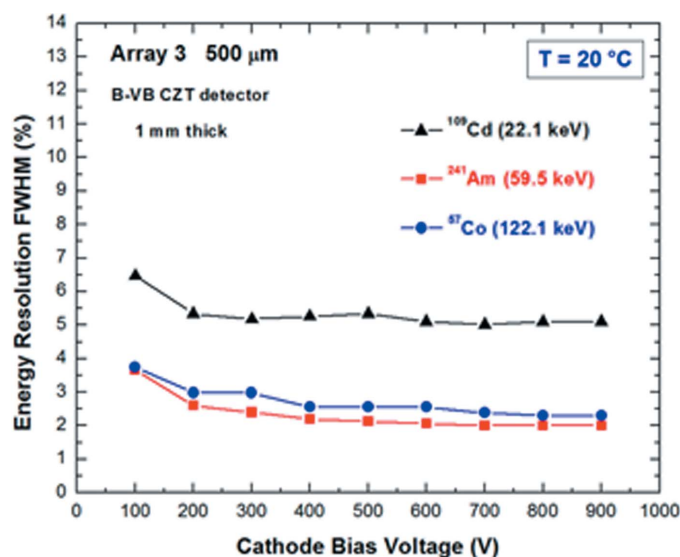
size and another set close to the detector to clean up any scattered X-rays. The detector system was mounted on a versatile optics table which can be moved in X, Y and Z directions with a precision of <1 µm. Line scans were automated using a TTL trigger generated by the B16 control system after each 10 µm step that began the data acquisition by the digitizers. Fig. 2(a) shows an overview of the experimental setup at the B16 beamline.

High-rate measurements were performed at the Livio Scarsi Laboratory (LAX) of the University of Palermo. A Seifert SN60 tube equipped with different targets (Ag, Co, Cr, Cu, Fe, Mo and W) allows the production of X-rays in the 1–60 keV energy range and with fluence rates of 10^5–10^8 photons mm^{-2} s^{-1} (Principato et al., 2015). In this work, X-rays from a Mo target were used. The experimental setup used at LAX is shown in Fig. 2(b). All measurements were performed at room temperature ($T = 20°$C).

3. Low-rate measurements

3.1. Spectroscopic response to uncollimated radiation sources and charge-transport properties

An overview of the low-rate performance of the detectors at different bias voltages is shown in Fig. 3. In particular, we present the energy-resolution (FWHM) values versus the cathode bias voltage at different energies, i.e. at 22.1 keV (^{109}Cd source), at 59.5 keV (^{241}Am source) and at 122.1 keV (^{57}Co source). The energy spectra were measured at input counting rates (ICRs) of less than 600 cps (counts per second). The results highlight the high-bias-voltage operation (9000 V cm^{-1}) of the detectors even at room temperature; this is because of the good electric characteristics of these detectors which, despite the quasi-ohmic contacts of the electrodes,

Figure 2
(a) The experimental setup used for the micro-beam characterization of the detectors at the B16 beamline of the Diamond Light Source. (b) The experimental setup used for high-rate measurements at the Livio Scarsi Laboratory.

Figure 3
Room-temperature energy resolution (FWHM) of a selected pixel (pixel No. 8) of the large array 3 (500 µm) at different cathode bias voltages. The energy-resolution values of the detector at the main energies of uncollimated radiation sources are reported.

Array 3   500 µm
241Am source 900 V T = 20 °C
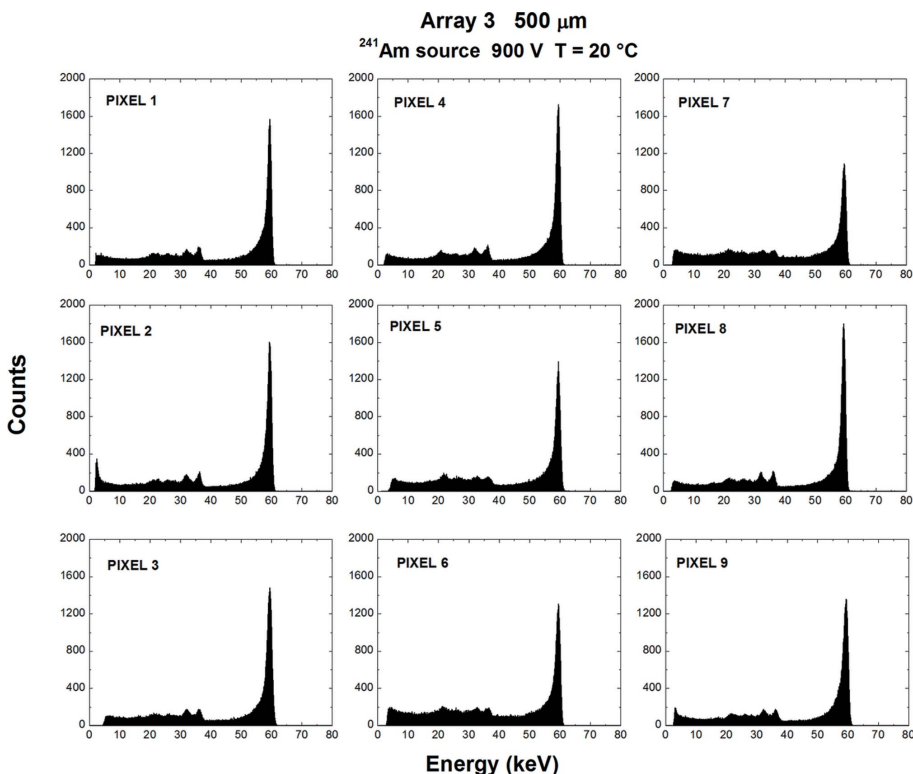
Figure 4
The measured [241]Am spectra of all nine pixels of the large array 3 (500 µm) at low-rate conditions (ICR = 500 cps). The energy resolution (FWHM) at 59.5 keV of the best pixel (pixel 8) and the sum of all the spectra are 2% (1.2 keV) and 2.5% (1.5 keV), respectively.

allow low-leakage currents, as already shown in previous investigations with planar detectors (Abbene *et al.*, 2016). Unfortunately, we cannot use cathode bias voltages higher than 900 V because of the electrical limits of the components of the bias-voltage filters. The measured [241]Am spectra of the nine pixels of the large array (array 3: pixel pitch of 500 µm)

are shown in Fig. 4. The measured [109]Cd and [57]Co spectra for the small array (array 0: pixel pitch of 250 µm) are also presented in Fig. 5. The detectors are characterized by excellent room-temperature energy-resolution values, as reported in Table 1.

The charge-carrier-transport properties were also investigated through the estimation of the mobility-lifetime product of the electrons ($\mu_e\tau_e$). To evaluate $\mu_e\tau_e$, we irradiated the detectors with the [109]Cd source from the cathode side and the energy spectra at different bias voltages were measured. The charge-collection efficiency (CCE) of a tested pixel at 22.1 keV versus the bias voltage is reported in Fig. 6. Typically, the estimation of $\mu_e\tau_e$ on planar detectors, where the weighting field can be considered uniform, is performed through the simplified Hecht equation (Sellin *et al.*, 2005). In pixel detectors, the presence of non-uniform weighting potential and electric field (Barret *et al.*, 1995; Zanichelli *et al.*, 2012) limits the application of the Hecht equation in the estimation of $\mu_e\tau_e$. To account for these non-uniformities, we modelled the CCE through the following equation based on the Shockley–Ramo theorem (He, 2001),

$$\mathrm{CCE} = \int_0^L \exp\left[-\frac{x}{\mu\tau E(x)}\right] W(x)\,\mathrm{d}x, \qquad (1)$$
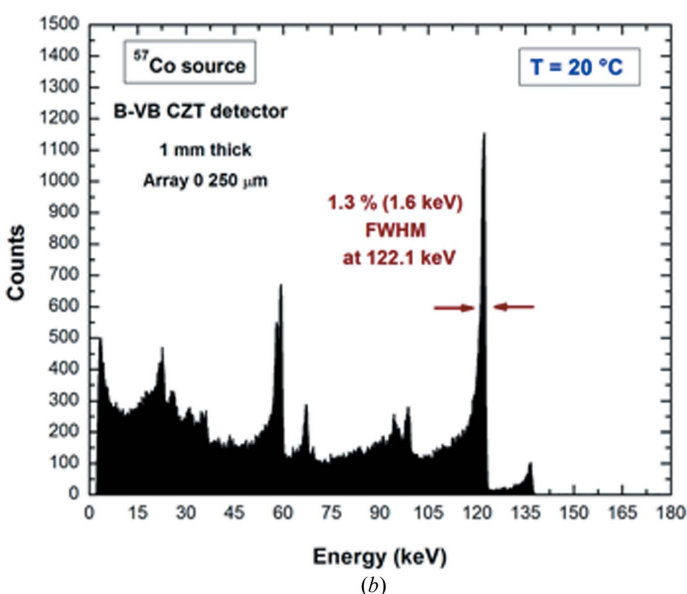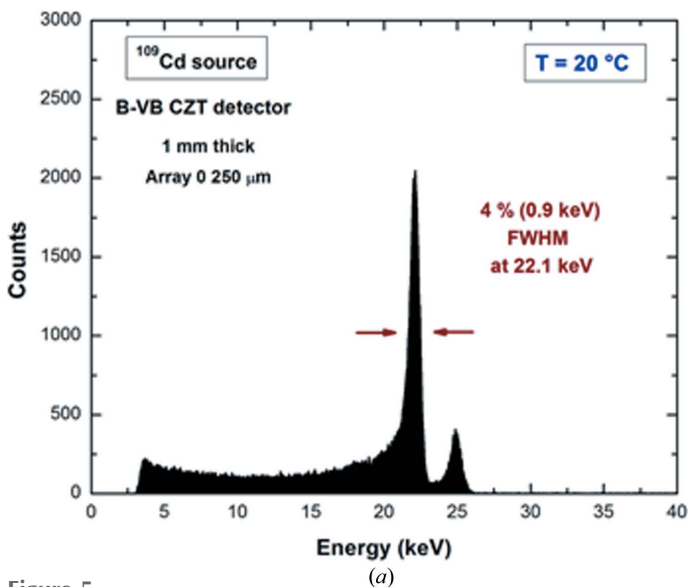
Figure 5
Measured energy spectra of uncollimated (*a*) [109]Cd and (*b*) [57]Co sources of pixel 4 of the array 0 (pixel pitch of 250 µm) at low-rate conditions (<600 cps). We measured energy-resolution (FWHM) values of 4% (0.9 keV) and 1.3% (1.6 keV) at 22.1 and 122.1 keV, respectively.

Table 1
Energy resolution (FWHM) at different energies with a bias voltage of 900 V at $T = 20°C$.

The Fano noise was calculated by using a Fano factor $F = 0.1$ (Devanathan *et al.*, 2006; Kuvvetli & Budtz-Jørgensen, 2005; Owens *et al.*, 2004).

Array	Pixel	Energy resolution at 22.1 keV (keV) Fano noise: 0.2 keV	Energy resolution at 59.5 keV (keV) Fano noise: 0.4 keV	Energy resolution at 122.1 keV (keV) Fano noise: 0.6 keV
Array 3 (500 µm)	Best pixel (No. 8)	1.1 (5.1%)	1.2 (2.0%)	2.8 (2.3%)
Array 3 (500 µm)	Sum of all spectra	1.3 (5.8%)	1.5 (2.5%)	3.7 (3.0%)
Array 0 (250 µm)	Best pixel (No. 4)	0.9 (4%)	1.0 (1.7%)	1.6 (1.3%)
Array 0 (250 µm)	Sum of all spectra	1.0 (4.5%)	1.2 (2%)	2.3 (1.9%)
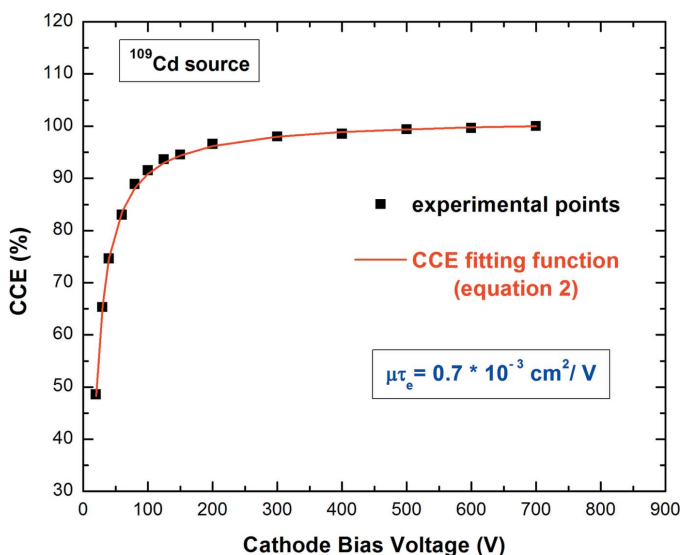
Figure 6
CCE of a selected pixel at various cathode bias voltages. The fitting function [equation (2)] takes into account the non-uniform behaviour of both the weighting and the electric fields.

where x is the interaction depth, L is the detector thickness, $W(x)$ is the weighting field and $E(x)$ is the electric field. By simulating the weighting field $W(x)$ of a pixel detector (COMSOL Multiphysics) and by modelling the electric field $E(x)$ with a linear behaviour (Zanichelli *et al.*, 2012), the CCE can be written as follows.

$$CCE(V) = \int_0^L \exp\left(-\frac{x}{\mu\tau\{(V/L) + \alpha[x - (L/2)]\}}\right) W(x)\,dx,$$
(2)

where α is the slope of the linear behaviour of the electric field $E(x)$ and V is the bias voltage used. Through a best-fitting procedure with equation (2), we estimated $\mu_e\tau_e$ values ranging from 0.6 to 0.7×10^{-3} cm^2 V^{-1} (α values between -1.9 and -2×10^3 V cm^{-2}).

3.2. Spectroscopic response to collimated synchrotron X-rays

Fig. 7 shows the spectroscopic response of the detectors to mono-energetic synchrotron X-rays. In particular we irradiated the centre of each pixel with collimated X-ray beams (75 µm × 75 µm) at energies below (20 keV) and above (50 keV) the K-shell absorption energy of the CZT material

(26.7 keV, 9.7 keV and 31.8 keV for Cd, Zn and Te, respectively). The excellent room-temperature performance is clearly shown, with energy-resolution values of 3.3% (0.66 keV) and 1.5% (0.75 keV) FWHM at 20 keV and 50 keV, respectively. At 50 keV, the escape peaks are clearly visible in the spectra: the 26.8 keV peak is caused by the escape of the Cd $K\alpha$ fluorescent line (23.2 keV), the second peak (between 23.9 and 22.5 keV) is caused by the escape of the Cd $K\beta$ and Te $K\alpha$ fluorescent lines (26.1 and 27.5 keV), while the third peak at 19 keV is caused by the escape of the Te K_β fluorescent line (31 keV).

To investigate the presence of non-uniformities, we also performed a 2D mapping of the detectors. To do this, a 10 µm × 10 µm micro-beam was scanned across the detectors for both the 500 and 250 µm pitch arrays, with scan steps of 25 and 12.5 µm, respectively. The results of the mapping are shown in Fig. 8, where the 40 keV photopeak energy at different positions is presented. Variations in the photopeak energy are mainly confined near the inter-pixel gaps because of charge-sharing effects (as will be described in the next section). The violet squares are caused by acquisition failures.

3.3. Charge-sharing measurements

As well documented in the literature (Bolotnikov *et al.*, 2005; Guerra *et al.*, 2008), sub-millimetre CZT pixel detectors typically suffer from charge sharing and cross-talk distortions. These phenomena mainly occur in the region near the inter-pixel gaps of the detector arrays. In particular, charge sharing is referred to as the splitting of the electron-charge cloud generated from a single photon and collected by the neighbouring pixels. The area over which the charge cloud is deposited depends upon geometrical (pixel and inter-pixel gap size) and physical properties (charge diffusion, electric field distortions, Coulomb repulsion, K-shell X-ray fluorescence, Compton scattering). Cross-talk events between neighbouring pixels are created by K-shell X-ray fluorescence, Compton scattering and induced-charge pulses (Guerra *et al.*, 2008; Brambilla *et al.*, 2012; Bolotnikov *et al.*, 2016; Kim *et al.*, 2011; Zhu *et al.*, 2011). Degradation of the energy resolution, the presence of fluorescence/escape peaks and an increase in the low-energy background are the main distortions in the measured spectra. The detection of charge-sharing events is typically performed by analysing the events of a pixel that is in temporal coincidence with neighbouring pixels. This technique is generally termed time-coincidence analysis. We performed

charge-sharing measurements in our detectors with both uncollimated and collimated X-ray beams. Fig. 9(a) shows the number of coincidence events of the central pixel of the large and small arrays with eight adjacent pixels at different coincidence-time windows (CTWs). The energy spectra (uncollimated ^{241}Am source) of the coincidence events are also presented in Fig. 9(b). Because of the higher gap/pixel area ratio, the small array (array 0) is characterized by more charge-sharing events. Almost all shared events (90%) are detected within a CTW of 20 ns and the saturation of the curves clearly shows the full detection of the shared events within the investigated CTW range. The percentages of charge-shared events of the central pixel for the small and large arrays are summarized in Table 2.

The higher percentage of charge-sharing events at energies (^{241}Am source) above the K-shell absorption energy of the CZT material highlights the critical role of the X-ray fluorescence. Fluorescent X-rays increase the broadening of the initial charge cloud and they create cross-talk events between adjacent pixels. The effects of rejecting the shared events in the energy spectra, i.e. after charge-sharing discrimination (CSD), are shown in Fig. 10. After CSD, the low-energy background and the fluorescent X-rays are deleted in the energy spectrum. The presence of escape peaks after CSD is caused by the back-escape events (e.g. from the cathode side).

Despite the benefits of CSD in the measured spectra, this technique produces a strong reduction in the throughput of the detectors, as reported in Table 2. To recover the rejected events after CSD the charge-sharing addition (CSA) technique is typically applied. This approach consists of summing the energies of the coincidence events. However, as documented in the literature (Abbene et al., 2015a, 2018a; Allwork et al., 2012; Brambilla et al., 2012; Bolotnikov et al., 1999, 2002; Gaskin et al., 2003; Kalemci et al., 2002; Kim et al., 2011; Kuvvetli & Budtz-Jørgensen, 2007), the presence of charge losses at the inter-pixel gap often limited the application of CSA in CdTe/CZT pixel detectors. After applying CSA in our detectors, we observed charge/energy losses in the summed spectra between two adjacent pixels. For example, as shown in Fig. 11(a), the main peak at 59.5 keV after CSA (black line) is characterized by an energy loss of about 2.5 keV. As presented in our
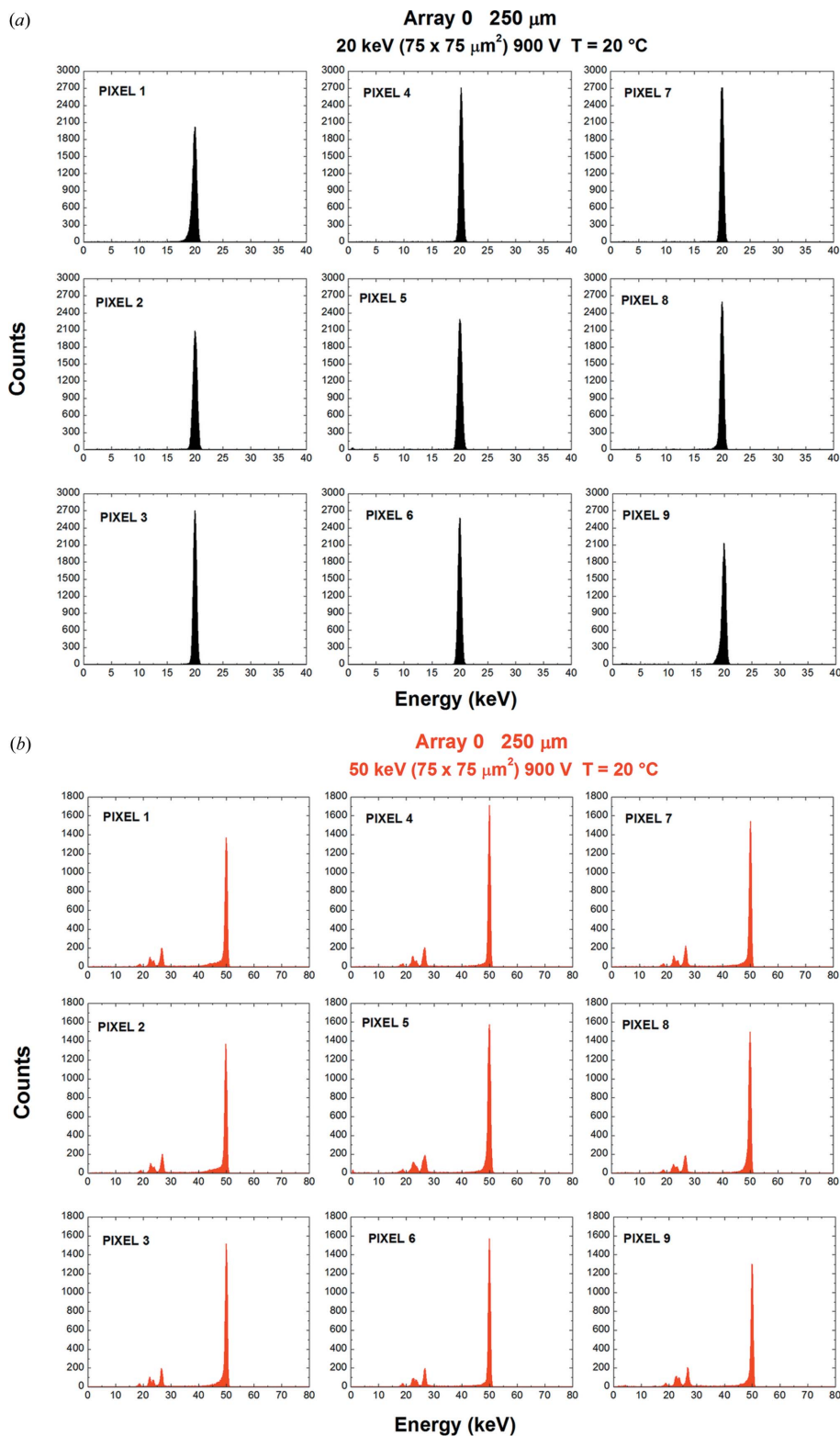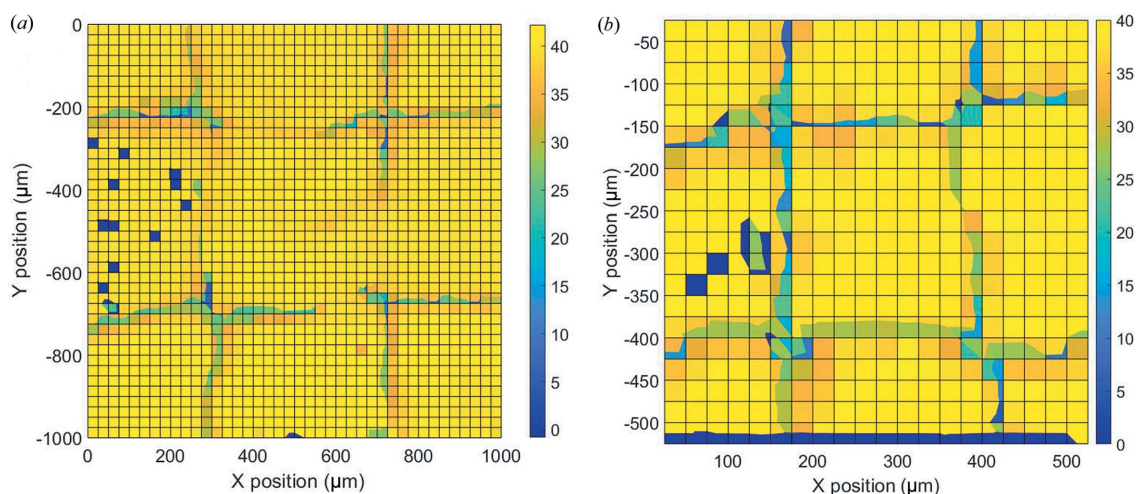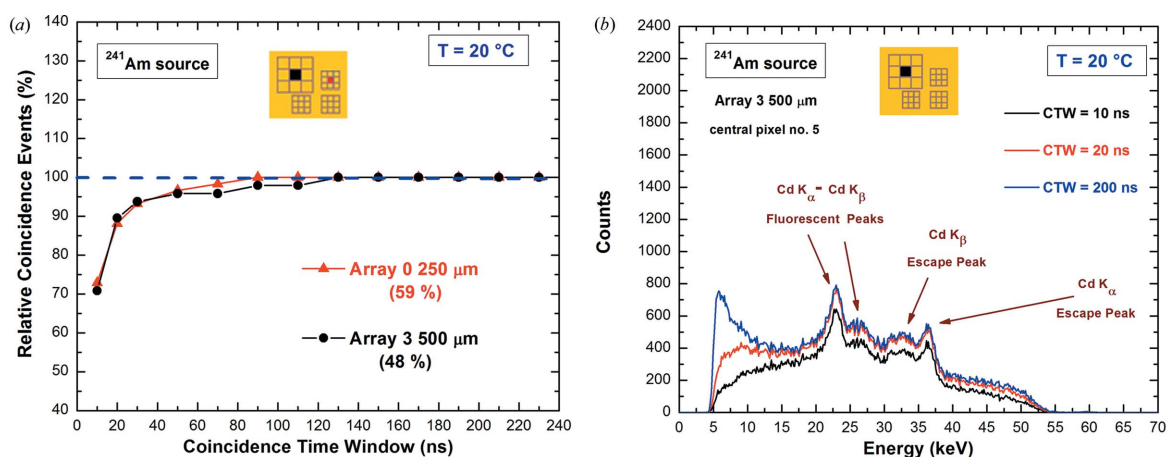

Figure 7
The measured energy spectra for mono-energetic synchrotron X-rays collimated at the centre of each pixel (75 μm × 75 μm). Energy spectra (a) at 20 keV and (b) at 50 keV.
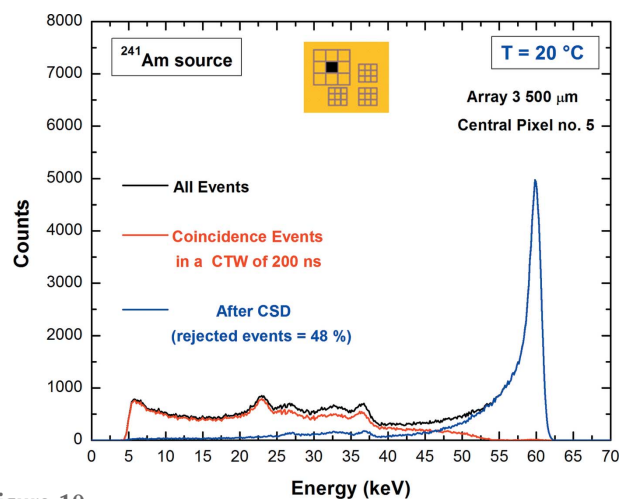
Figure 8
The results of a 2D synchrotron mapping for the large (*a*) and small (*b*) pixel arrays at 40 keV. The changes in the photopeak energy are confined near the inter-pixel gaps because of charge-sharing effects. The violet squares are caused by acquisition failures.
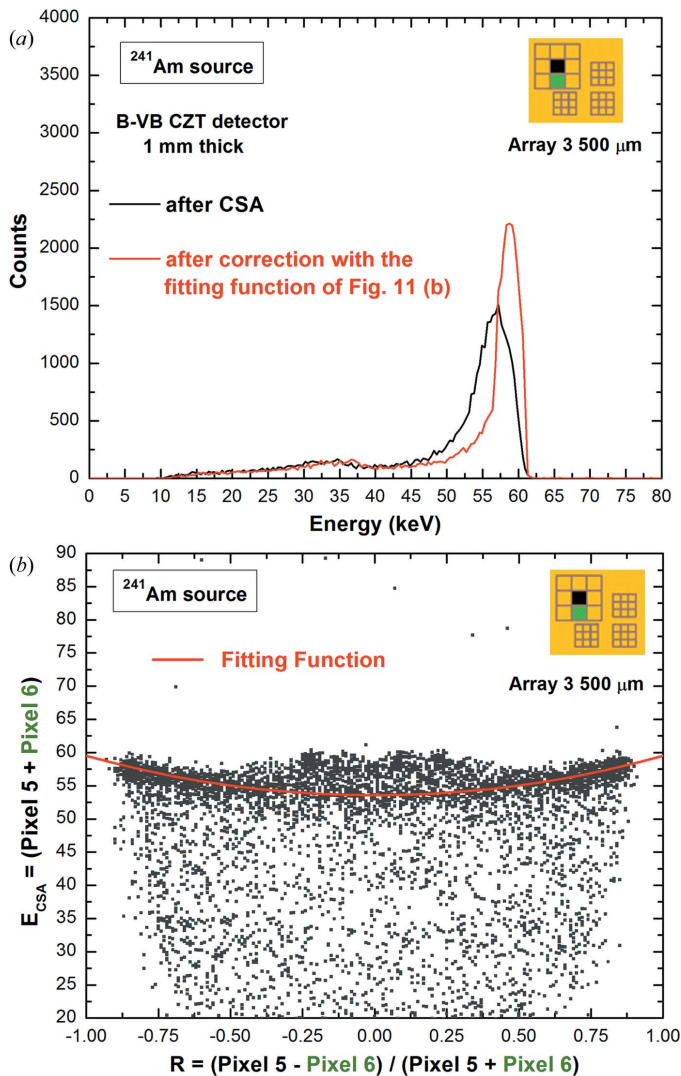

Figure 9
(*a*) Relative coincidence events (percentage) of the central pixel (pixel No. 5) with the adjacent pixels at different CTWs (uncollimated ^{241}Am source). An energy threshold of 4 keV for all pixels was used. The percentage values of the coincidence events of the central pixel with all eight pixels are also shown (CTW of 200 ns). (*b*) The energy spectra of the coincidence events of the central pixel at three different CTWs. Examples of fluorescent and escape peaks are clearly visible.

previous work (Abbene *et al.*, 2018*b*; Bugby *et al.*, 2019), this energy deficit can be recovered by using a function which fits the 2D scatter plot of the energy E_{CSA} after CSA versus the sharing ratio R [Fig. 11(*b*)]. The corrected spectrum (red line) is shown in Fig. 11(*a*). A detailed description of this correction technique is reported in a previous work (Abbene *et al.*, 2018*b*).

A micro-beam characterization of charge-sharing effects was also performed. Collimated synchrotron X-rays were used to investigate charge-sharing and charge-loss effects on a sub-pixel level. The results of a microscale line scanning between the centres of two adjacent pixels (pixels 5 and 6) of the small array are presented. We used collimated (10 μm × 10 μm) synchrotron X-ray beams with energies below (25 keV) and above (40 keV) the *K*-shell absorption energy of CZT material, with position steps of 12.5 μm. During the line scanning between the two pixels, we acquired, at each beam position, the data from all nine pixels of the investigated array. Fig. 12 shows an overview of the variation of the photopeak centroid

Figure 10
The measured ^{241}Am spectrum of the central pixel of the large array after CSD (blue line). The raw spectrum of the central pixel (black line) and the spectrum of the coincidence events with all eight adjacent pixels (red line) are also shown.

Table 2
Charge-sharing percentages between the central pixel and the eight adjacent pixels of the pixel arrays at $T = 20°C$.

The shared events are detected within a CTW of 200 ns and with an energy threshold of 4 keV.

Detector	Pixel pitch	Sharing percentages at 22.1 keV (%)	Sharing percentages at 59.5 keV (%)
B-VB	500 µm	22	48
1 mm-thick (900 V)	250 µm	25	59

other pixels ($m > 2$). The presence of charge losses after CSA was also confirmed with the collimated beams at the centre of the inter-pixel gap.

4. High-rate measurements

The spectroscopic response of the detectors was also measured at high-rate conditions. The aim was to investigate the presence of high-flux radiation polarization effects in the detectors. Mo-target X-ray spectra (main fluorescent lines at 17.5 and 19.6 keV) were measured at different rates (Fig. 13). The measured spectra (central pixel of the large array) show no energy shifts and low spectroscopic degradation up to 600 kcps; this is mainly because of the high-rate ability of the digital electronics, which minimizes both baseline shift and peak pile-up effects in the spectra. However, no polarization effects were observed up to the investigated fluence-rate conditions (2.2×10^6 photons mm^{-2} s^{-1}).
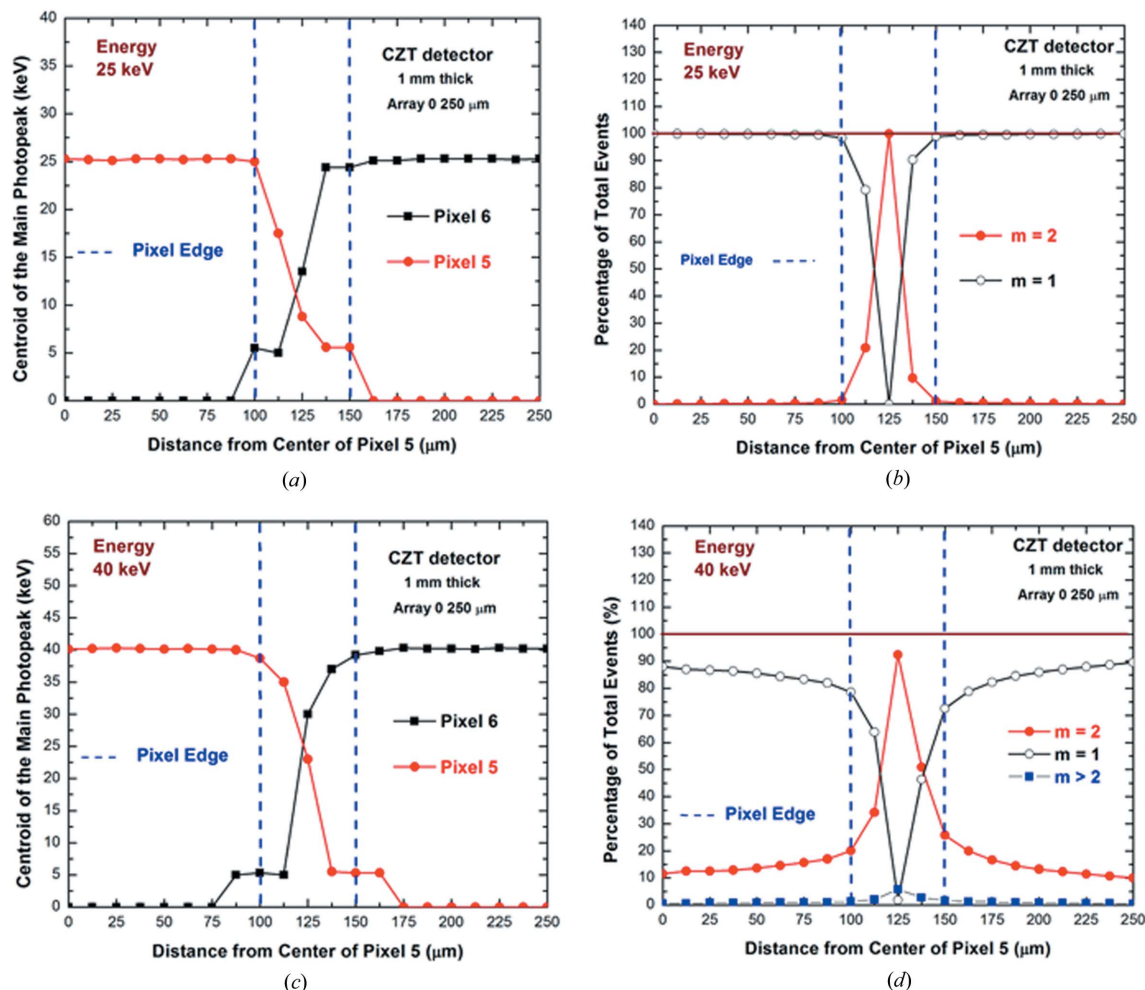
5. Conclusions

The performances of new CZT pixel detectors were presented in this work. Sub-millimetre pixel detectors (pixel pitches of 500 and 250 µm) were fabricated, based on CZT crystals grown by the B-VB technique (IMEM-CNR). The detectors show excellent room-temperature performance at high-bias-voltage conditions (electric field of 9000 V cm^{-1}), with energy-resolution values of 1 keV (FWHM) at 60 keV. Charge-sharing measurements, with uncollimated and collimated beams, highlighted the presence of charge losses near the inter-pixel regions. The absence of high-flux radiation-induced polarization effects was also observed up to fluence rates of 2.2×10^6 photons mm^{-2} s^{-1}.

Figure 11
(a) The energy spectrum after CSA (black line) and after the proposed correction technique (red line) with the fitting function of Fig. 11(b). (b) 2D scatter plot of the energy E_{CSA} of the coincidence events ($m = 2$), between pixels 5 and 6, after CSA. The energy E_{CSA} is plotted versus the charge-sharing ratio R, which gives information about the interaction position of the events. The red line represents the best-fitting function used to correct charge losses after CSA.

of the main peaks (25 keV and 40 keV) and the multiplicity m with changing beam position. At 25 keV, centroid variations are observed in a region of 50 µm centred on the middle of the inter-pixel region. Coincidence events ($m > 1$) were only detected at beam positions within 50 µm of the centre of the inter-pixel region. At the centre of the inter-pixel gap, 100% of events were shared between the two pixels. At 40 keV, coincidence events were detected in a wider region, even for beam positions near the centre of the pixels. This is because of the propagation of fluorescent X-rays that increases the initial charge cloud and creates cross-talk events. The attenuation lengths of the Cd $K\alpha$ and Cd $K\beta$ X-rays are 116 and 161 µm, respectively (Abbene et al., 2018a,b; Allwork et al., 2012). At the centre of the inter-pixel gap, 93% of the events are shared between pixels 5 and 8 ($m = 2$), while 6% are shared with the

Figure 12

Microscale line scanning (position steps of 12.5 μm) between the centres of two adjacent pixels (pixels 5 and 6) at energies below (25 keV) and above (40 keV) the *K*-shell absorption energy of CZT material. Photopeak centroids, (*a*) and (*c*), and multiplicity *m*, (*b*) and (*d*), at various positions. The jump discontinuities visible in the curves for peak centroid values around 5 keV are caused by the non-zero energy threshold (4 keV).
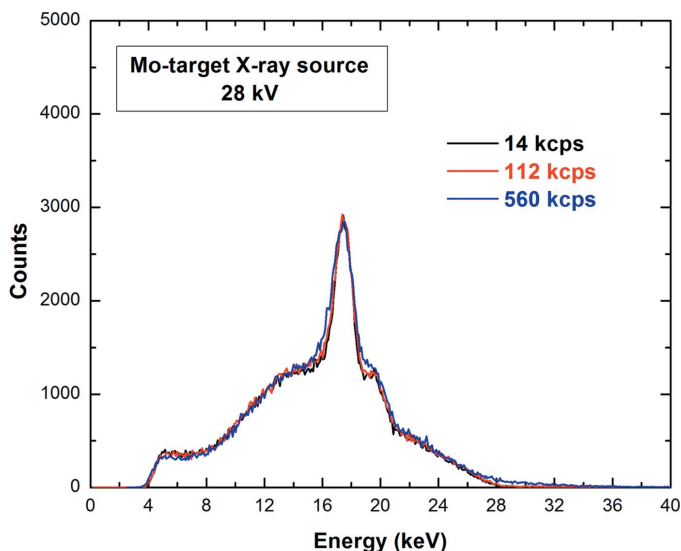
Figure 13

Measured Mo-target X-ray spectra (central pixel of the large array) at different ICRs.

References

Abbene, L. & Gerardi, G. (2015*b*). *J. Synchrotron Rad.* **22**, 1190–1201.

Abbene, L., Gerardi, G. & Principato, F. (2013*a*). *Nucl. Instrum. Methods Phys. Res. A*, **730**, 124–128.

Abbene, L., Gerardi, G. & Principato, F. (2015*a*). *Nucl. Instrum. Methods Phys. Res. A*, **777**, 54–62.

Abbene, L., Gerardi, G., Principato, F., Bettelli, M., Seller, P., Veale, M. C., Fox, O., Sawhney, K., Zambelli, N., Benassi, G. & Zappettini, A. (2018*b*). *J. Synchrotron Rad.* **25**, 1078–1092.

Abbene, L., Gerardi, G., Turturici, A. A., Del Sordo, S. & Principato, F. (2013*b*). *Nucl. Instrum. Methods Phys. Res. A*, **730**, 135–140.

Abbene, L., Gerardi, G., Turturici, A. A., Raso, G., Benassi, G., Bettelli, M., Zambelli, N., Zappettini, A. & Principato, F. (2016). *Nucl. Instrum. Methods Phys. Res. A*, **835**, 1–12.

Abbene, L., Principato, F., Gerardi, G., Bettelli, M., Seller, P., Veale, M. C., Zambelli, N., Benassi, G. & Zappettini, A. (2018a). *J. Synchrotron Rad.* **25**, 257–271.

Allwork, C., Kitou, D., Chaudhuri, S., Sellin, P. J., Seller, P., Veale, M. C., Tartoni, N. & Veeramani, P. (2012). *IEEE Trans. Nucl. Sci.* **59**, 1563–1568.

Barber, W. C., Wessel, J. C., Nygard, E. & Iwanczyk, J. S. (2015). *Nucl. Instrum. Methods Phys. Res. A*, **784**, 531–537.

Barret, H. H., Eskin, J. D., Barber, H. B. (1995). *Phys. Rev. Lett.* **75**, 156–159.

Bolotnikov, A. E., Boggs, S. E., Hubert Chen, C. M., Cook, W. R., Harrison, F. A. & Schindler, S. M. (2002). *Nucl. Instrum. Methods Phys. Res. A*, **482**, 395–407.

Bolotnikov, A. E., Camarda, G. S., Cui, Y., De Geronimo, G., Eger, J., Emerick, A., Fried, J., Hossain, A., Roy, U., Salwen, C., Soldner, S., Vernon, E., Yang, G. & James, R. B. (2016). *Nucl. Instrum. Methods Phys. Res. A*, **805**, 41–54.

Bolotnikov, A. E., Camarda, G. C., Wright, G. W. & James, R. B. (2005). *IEEE Trans. Nucl. Sci.* **52**, 589–598.

Bolotnikov, A. E., Cook, W. R., Harrison, F. A., Wong, A., Schindler, S. M. & Eichelberger, A. C. (1999). *Nucl. Instrum. Methods Phys. Res. A*, **432**, 326–331.

Brambilla, A., Ouvrier-Buffet, P., Rinkel, J., Gonon, G., Boudou, C. & Verger, L. (2012). *IEEE Trans. Nucl. Sci.* **59**, 1552–1558.

Bugby, S. L., Koch-Mehrin, K. A., Veale, M. C., Wilson, M. D. & Lees, J. E. (2019). *Nucl. Instrum. Methods Phys. Res. A*, **940**, 142–151.

Chen, H., Awadalla, S. A., Iniewski, K., Lu, P. H., Harris, F., Mackenzie, J., Hasanen, T., Chen, W., Redden, R., Bindley, G., Kuvvetli, I., Budtz-Jørgensen, C., Luke, P., Amman, M., Lee, J. S., Bolotnikov, A. E., Camarda, G. S., Cui, Y., Hossain, A. & James, R. B. (2008). *J. Appl. Phys.* **103**, 014903.

Del Sordo, S., Abbene, L., Caroli, E., Mancini, A. M., Zappettini, A. & Ubertini, P. (2009). *Sensors*, **9**, 3491–3526.

Del Sordo, S., Strazzeri, M., Agnetta, G., Biondo, B., Celi, F., Guarrusso, S., Mangano, A., Russo, F., Caroli, E., Donati, A., Schiavone, F., Stephen, J. B., Ventura, G., Abbene, L., Fauci, F., Raso, G. & Pareachi, G. (2004). *Nuovo Cimento B*, **119**, 257–270.

Devanathan, R., Corrales, L. R., Gao, F. & Weber, W. J. (2006). *Nucl. Instrum. Methods Phys. Res. A*, **565**, 637–649.

Farella, I., Montagna, G., Mancini, A. M. & Cola, A. (2009). *IEEE Trans. Nucl. Sci.* **56**, 1736–1742.

Fougeres, P., Siffert, P., Hageali, M., Koebel, J. M. & Regal, R. (1999). *Nucl. Instrum. Methods Phys. Res. A*, **428**, 38–44.

Gaskin, J. A., Sharma, D. P. & Ramsey, B. D. (2003). *Nucl. Instrum. Methods Phys. Res. A*, **505**, 122–125.

Gerardi, G. & Abbene, L. (2014). *Nucl. Instrum. Methods Phys. Res. A*, **768**, 46–54.

Guerra, P., Santos, A. & Darambara, D. G. (2008). *Phys. Med. Biol.* **53**, 1099–1113.

He, Z. (2001). *Nucl. Instrum. Methods Phys. Res. A*, **463**, 250–267.

Iniewski, K. (2014). *J. Instrum.* **9**, C11001.

Iwanczyk, J., Nygård, E., Meirav, O., Arenson, J., Barber, W. C., Hartsough, N. E., Malakhov, N. & Wessel, J. C. (2009). *IEEE Trans. Nucl. Sci.* **56**, 535–542.

Kalemci, E. & Matteson, J. L. (2002). *Nucl. Instrum. Methods Phys. Res. A*, **478**, 527–537.

Kim, J. C., Anderson, S. E., Kaye, W., Zhang, F., Zhu, Y., Kaye, S. J. & He, Z. (2011). *Nucl. Instrum. Methods Phys. Res. A*, **654**, 233–243.

Knoll, G. F. (2000). *Radiation Detection and Measurement*, 3rd ed., ch. 16, pp. 599–601. New York: John Wiley and Sons.

Kuvvetli, I. & Budtz-Jørgensen, C. (2005). *IEEE Trans. Nucl. Sci.* **52**, 1975–1981.

Kuvvetli, I. & Budtz-Jørgensen, C. (2007). *IEEE Nucl. Sci. Symp. Conf. Rec.* **3**, 2252–2257.

McGregor, D. S. & Hermon, H. (1997). *Nucl. Instrum. Methods Phys. Res. A*, **395**, 101–124.

Owens, A. & Peacock, A. (2004). *Nucl. Instrum. Methods Phys. Res. A*, **531**, 18–37.

Principato, F., Gerardi, G., Turturici, A. A., Raso, G., Quartararo, M., Pintacuda, F. & Abbene, L. (2015). *Proceedings of the 15th European Conference on Radiation and its Effects on Components and Systems* (*RADECS*). 7365672. IEEE.

Principato, F., Turturici, A. A., Gallo, M. & Abbene, L. (2013). *Nucl. Instrum. Methods Phys. Res. A*, **730**, 141–145.

Schneider, A., Veale, M. C., Duarte, D. D., Bell, S. J., Wilson, M. D., Lipp, J. D. & Seller, P. (2015). *J. Instrum.* **10**, C02010.

Seller, P., Bell, S., Cernik, R. J., Christodoulou, C., Egan, C. K., Gaskin, J. A., Jacques, S., Pani, S., Ramsey, B. D., Reid, C., Sellin, P. J., Scuffham, J. W., Speller, R. D., Wilson, M. D. & Veale, M. C. (2011). *J. Instrum.* **6**, C12009.

Sellin, P. J., Davies, A. W., Lohstroh, A., Ozsan, M. E. & Parkin, J. (2005). *IEEE Trans. Nucl. Sci.* **52**, 3074–3078.

Szeles, C., Soldner, S. A., Vydrin, S., Graves, J. & Bale, D. S. (2008). *IEEE Trans. Nucl. Sci.* **55**, 572–582.

Takahashi, T. & Watanabe, S. (2001). *IEEE Trans. Nucl. Sci.* **48**, 950–959.

Turturici, A. A., Abbene, L., Gerardi, G. & Principato, F. (2014). *Nucl. Instrum. Methods Phys. Res. A*, **763**, 476–482.

Van Herdeen, P. J. (1945). PhD Dissertation. Rijiksuniversiteit Utrecht, The Netherlands.

Veale, M. C., Bell, S. J., Duarte, D. D., French, M. J., Hart, M., Schneider, A., Seller, P., Wilson, M. D., Kachkanov, V., Lozinskaya, A. D., Novikov, V. A., Tolbanov, O. P., Tyazhev, A. & Zarubin, A. N. (2014). *J. Instrum.* **9**, C12047.

Veale, M. C., Bell, S. J., Jones, L. L., Seller, P., Wilson, M. D., Allwork, C., Kitou, D., Sellin, P. J., Veeramani, P. & Cernik, R. C. (2011). *IEEE Trans. Nucl. Sci.* **58**, 2357–2362.

Zanichelli, M., Pavesi, M., Marchini, L. & Zappettini, A. (2012). *Solid State Commun.* **152**, 1212–1215.

Zappettini, A., Zha, M., Marchini, L., Calestani, D., Mosca, R., Gombia, E., Zanotti, L., Zanichelli, M., Pavesi, M., Auricchio, N. & Caroli, E. (2009). *IEEE Trans. Nucl. Sci.* **56**, 1743–1746.

Zappettini, A., Zha, M., Pavesi, M. & Zanotti, L. (2007). *J. Cryst. Growth*, **307**, 283–288.

Zhang, F., He, Z. & Seifert, C. E. (2007). *IEEE Trans. Nucl. Sci.* **54**, 843–848.

Zhu, Y., Anderson, S. E. & He, Z. (2011). *IEEE Trans. Nucl. Sci.* **58**, 1400–1409.